
IMPROVING LANDSLIDE DETECTION ON SAR DATA THROUGH DEEP LEARNING

Lorenzo Nava

Department of Earth Sciences
University of Florence
Florence 50121, Italy
lorenzo.nava@stud.unifi.it

Oriol Monserrat

Department of Remote Sensing
Centre Tecnològic Telecomunicacions Catalunya
Castelldefels 08860, Spain
omonserrat@cttc.cat

Filippo Catani

Department of Geosciences
University of Padua
Padua 35131, Italy
filippo.catani@unipd.it

May 4, 2021

ABSTRACT

In this letter, we use deep-learning convolution neural networks (CNNs) to assess the landslide mapping and classification performances on optical images (from Sentinel-2) and SAR images (from Sentinel-1). The training and test zones used to independently evaluate the performance of the CNNs on different datasets are located in the eastern Ihuri subprefecture in Hokkaido, where, at 03.08 local time (JST) on September 6, 2018, an Mw 6.6 earthquake triggered about 8000 coseismic landslides. We analyzed the conditions before and after the earthquake exploiting multi-polarization SAR as well as optical data by means of a CNN implemented in TensorFlow that points out the locations where the Landslide class is predicted as more likely. As expected, the CNN run on optical images proved itself excellent for the landslide detection task, achieving an overall accuracy of 99.20% while CNNs based on the combination of ground range detected (GRD) SAR data reached overall accuracies beyond 94%. Our findings show that the integrated use of SAR data may also allow for rapid mapping even during storms and under dense cloud cover and seems to provide comparable accuracy to classical optical change detection in landslide recognition and mapping.

Keywords Landslides · deep learning (DL) · convolution neural networks(CNNs) · image classification · remote sensing (RS) · Sentinel-1 · Sentinel-2 · landslide detection · synthetic aperture radar (SAR) · Tensorflow.

1 Introduction

In the world, several natural phenomena, like earthquakes and intense rainfalls, sometimes combined with windstorms, can trigger multiple landslide events, that can occur in groups of hundreds or even thousands in a region [1-5]. Those events can cause noticeable damages to natural and human infrastructures and can cause physical damages and heavy economic and social impacts [6]. Therefore, there is a growing need to intervene quickly and efficiently in the affected areas. Numerous techniques have been elaborate to produce susceptibility maps [7], [8], and mitigation strategies [9], [10]. Undoubtedly, in the case of multiple occurrences of landslides over a large area, the most common mapping method relies on remote sensing data because of its potential to quickly mapping geological features of whole regions, without physical contact with the areas investigated. A vast amount of research exists that has been performed to this end with knowledge-based methods, multiple regression, analytic hierarchy process [11], and machine learning (ML) techniques [12-15]. However, as time is a key factor when mapping natural disaster effects [16], usage of optical data alone can have serious limitations in presence of cloud cover. A possible solution, offered by the usage of SAR satellites,

has been exploited only scantily, so far, because landslide mapping algorithms have been mainly developed to run on optical data together with ancillary geological and topographic stationary information and because SAR data require specific analysis methods and classification algorithms, not yet fully developed for mass movements on natural slopes. Therefore, a research gap is still present in the lack of reliable image analysis methods to extract landslide mapping information from SAR images. Furthermore, it is not available, in the bibliography, an automatic method that employs the combination of CNNs and SAR data to extract spatial landslide information, probably due to the characteristics of the SAR data, which provides different information compared to the mainly exploited optical data, making essential the development of innovative techniques. Recently, deep learning (DL) approaches and, mainly, convolutional neural networks (CNNs) have been used in various remote sensing tasks on VHR imagery, such as classification, segmentation [17], and object detection [18]. Nevertheless, few are the studies that use CNNs for landslide detection. Ding et al. [19] carried out an automatic recognition of landslide at pixel scale based on CNNs on GF-1 images with four spectral bands (blue, green, red, and near-infrared) and a spatial resolution of 8 m, achieving a detection rate of 72.5%, a false positives rate of 10.2%, and overall accuracy of 67%. Ghorbanzadeh et al. [20] evaluated various ML algorithms on VHR optical data from the Rapid Wye satellite and topographic factors achieving 78.26% mIOU for a small window-size CNN. Another interesting study was carried out by Catani [21], in which the author evaluates different state-of-art CNNs on non-nadir and crowdsourced optical images of landslides to classify them, achieving overall accuracies between 87% and 90%. Indeed, optical images are great tools, but they present limitations due to the cloud cover that, in regions as the Congo River basin, Equatorial South America, and Southeast Asia, can display annual cloud frequencies higher than 80% [22]. In some cases, the first cloudless image available in the service after multiple landslide events occurred about a month later, as happened in Chile in December 2017, in Nepal in 2015 [23], and in Ecuador in 2016. Despite numerous methods and techniques have been applied on SAR data to detect landslides, as can be seen in the review of Mondini et al. [24], our study is the first that provides, to this end, a DL-based method employing the combination of CNNs and SAR data. Furthermore, the accuracy achieved is comparable to optical change detection.

In the remainder of this letter, we show and discuss a deep-learning-based method to detect landslides also in case of illumination or atmospheric conditions not favorable for landform mapping. We used convolutional neural networks (CNNs) on various combinations of Sentinel-1 data and topographic factors. We apply CNN methods to landslide detection based on ground range detected (GRD) SAR imagery from the Sentinel-1 satellite, which, in a study carried out by Mondini et al. [20], showed unambiguous changes of amplitude caused by landslides in about eighty-four percent of the cases. Lastly, we compare the results obtained on eight different SAR-based datasets with an RGB dataset, and we provide the mapping of the study area by using the best models.

2 Study Area and Materials

Study Area Our case study area lies in the Iburi sub-prefecture of Hokkaido, Japan. It comprehends the Atsuma, Mukawa, and Abira towns, which present a specific population of less than 10,000 and a low population density of 17 inhabitants/km². The morphology of the area is composed mainly of hills. The maximum height is fewer than 800 m while the average elevation is 160 m. The basement complex of the region is mainly composed of sedimentary rocks of the Neogene tertiary system: layers of sandstone and mudstone, sandstone, conglomerate, and diatomaceous siltstone [26], [27]. In the study area, at 03.08 local time (JST) on September 6, 2018, struck an Mw 6.56 earthquake (HEIE). It was activated by a rupture of a low-activity blind fault with the epicenter located at 42.690 N 142.007 E [28]. The event triggered about 7837 coseismic landslides most of which occurred in locations where the elevation is less than 300 m [4]. The majority of the landslides slid down over the air-fall pumice and ash layers are shallow and are classified as planar type and spoon type [29].

Materials The Sentinel-1 mission encompasses two polar-orbiting satellites that perform C-band synthetic aperture radar imaging [30] while the Copernicus Sentinel-2 mission comprises two polar-orbiting satellites that sample 13 spectral bands: four bands at 10 m, six bands at 20 m, and three bands at 60 m spatial resolution [31]. We downloaded Sentinel-1 and Sentinel-2 images from the Copernicus Open Access Hub [32]. The first images (5 x 20 m) were acquired in Level-1 Ground Range Detected (GRD) mode, with VV and VH polarization, and Interferometric Wide (IW) acquisition mode. GRD products are focused SAR data that has been detected, multi-looked, and projected to ground range using an Earth ellipsoid model [33]. Images were acquired from three different days: a) 01 September 2018, b) 13 September 2018, c) 25 September 2018. Lastly, a Sentinel-2 VHR RGB image (10 x 10 m) was obtained from the first cloud-free day after the multiple landslide event (20 October 2018).

Surface topography is one of the most influential elements regarding landslides in hilly and mountainous areas and, above all, the slope angle is considered an essential component of slope stability analysis [34]. Therefore, in this study, we used a 30 m resolution digital elevation model (DEM) acquired from USGS Earth Explorer [35] and slope angle to

Table 1: Dates of Acquisition of Sentinel-2 and Sentinel-1 for the Study Area in Hokkaido in 2018.

Region and Year	Sentinel-2	Sentinel-1
Iburi, Hokkaido 2018	20-10	01-09
		13-09
		25-09

evaluate their impact on the SAR data. As quoted, we designed an RGB dataset and eight SAR-based datasets, each composed of different combinations of the data in Table 2, as described in Table 2.

Table 2: Composite images created with corresponding dataset name.

Dataset Name	Band1	Band2	Band3
RGB	Red	Green	Blue
SSD	VV after-event	VH after-event	DEM
SSS	VV after-event	VH after-event	Slope
BAD	VV before-event	VV after-event	DEM
BAS	VV before-event	VV after-event	Slope
HHH	VH before-event	VH after-event	VH after-event
BAA	VV before-event	VV after-event	VV after-event
BAC	VV before-event	VV after-event	VV after-event - VV before-event
BAH	VV before-event	VV after-event	VH after-event

3 Methodology

The radar information from Sentinel-1 is exploited in combination with topographic factors, to evaluate the performance of a CNN to detect landslides. The workflow of this study is as follow:

- Designing nine different datasets, one composed of RGB images, four composed by SAR data and a topographic factor as third band, of which two with slope and two with DEM, and four constituted only by SAR data.
- Training the CNN on each training dataset and validating the performance on the corresponding test dataset sampled in the study area.
- Visualizing the predictions of the best models on the entire study area.

In the following sections, we give a description and the results of this workflow. Additional information and considerations are provided in the conclusion section.

3.1 Dataset Pool

To create the datasets, each of the composite images in Table 2 is sampled in the GIS environment using the 'Export training data for deep learning' tool, that, after designing numerous polygons on known landslides, samples various clips per polygon with a predefined shape, stride, and resolution. The polygons position is chosen concerning the high variability of both classes, being careful to include various landslide shapes, orientations, and dimensions. Besides, we include different land covers, such as urban, wooded, and agricultural areas in the *Non-landslide* class. In all the datasets, the spatial resolution of the images is 25 x 25 pixels, which is equivalent to a spatial extension of 250 x 250 m for optical RGB images and 125 x 420 m for SAR products. We select this image size as the best size based on a cross-validation for our study area.

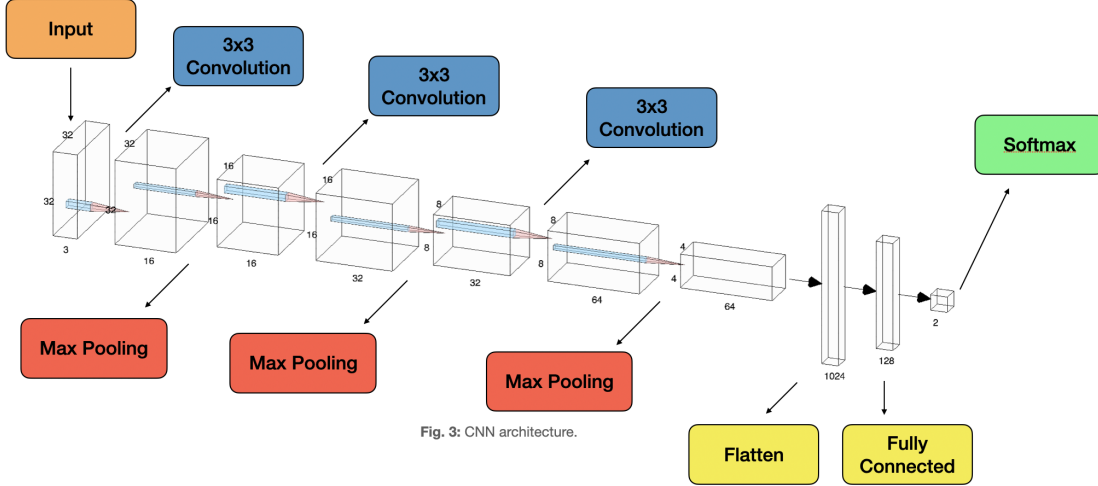


Figure 1: CNN architecture.

3.2 Supervised Classification

Recently, deep-learning methods and, above all, CNNs have accomplished reliable results in various tasks in computer vision, proving to be the state-of-art of this field [36], [37]. A CNN can autonomously learn hierarchical feature representations of an image, enabling it to perform classification tasks directly from images, e.g., recognizing a specific image without using human-designed features [38]. The peculiarity of a CNN is its architecture, which is composed of tens or hundreds of so-called hidden layers that exercise convolutional and pooling operations. During the training process, an input image flows through the network that scans it with a set of trainable kernels, resulting in a group of feature maps (forward phase), then gradients are back-propagated, and parameters are updated (backward phase). The output of each convolutional layer is filtered by an activation function (e.g., sigmoid, ReLU, Softmax, hyperbolic tangent) that performs non-linear transformations [39]. The pooling layer, usually placed after the convolutional layer, aims to simplify the output by performing non-linear down-sampling to reduce the parameters.

In this letter, we modify a network provided by the TensorFlow Core *Image Classification* library [40]. The model consists of three convolution blocks of 3x3 filters with a max pooling layer in each of them. Dropout and connected layer are activated by a ReLU activation function:

$$R(z) = \max(0, z) \quad (1)$$

The last fully connected layer has 2 units, as the number of classes we defined, and it is activated by a Softmax activation function:

$$\sigma(x)_j = \frac{e^{z_j}}{\sum_{k=1}^K e^{z_k}} \text{ for } j = 1, \dots, K \text{ and } z \in R \quad (2)$$

As loss function optimization, we used a stochastic gradient descent method based on an adaptive estimation of first-order and second-order moments (Adam), a method for problems with very noisy and/or sparse gradients [41]. Sparse Categorical Crossentropy (SCC) function is used as a loss function, which is an integer-based version of the Categorical Crossentropy function:

$$Loss = -\sum_{i=1}^M y_i \cdot \log \hat{y}_i \quad (3)$$

where \hat{y}_i is the i -th scalar value in the model output, y_i is the corresponding target value, and M , the output size is the number of scalar values in the model output. The SCC function computes the cross-entropy loss between the labels and predictions providing labels as integers [42]. The CNN is implemented using the Google's library TensorFlow [43]. Furthermore, many augmentation techniques are applied on the dataset, such as vertical and horizontal *Random Flip*, *Random Rotation*, *Random Zoom*, and *Random Translation*. Those are chosen considering that flipping, rotating, zooming, and translating a satellite landslide image results in new images of landslides with a possible real dimension and orientation. The trained model is used to predict classes on a labeled test dataset composed of images with the same number and type of bands of the training dataset. The output contains two classes, and accuracy (4), precision (5), and

recall (6) are calculated using these values according to the following formulas, where TP, TN, FP, and FN are true and false positives and negatives, respectively.

$$\text{Accuracy} = \frac{TP + TN}{TP + FP + TN + FN} \quad (4)$$

$$\text{Precision} = \frac{TP}{TP + FP} \quad (5)$$

$$\text{Recall} = \frac{TP}{TP + FN} \quad (6)$$

3.3 Object Detection

The study area is analyzed through the sliding window [44] method to detect landslides. The maps created are shown with superimposed the shapefile of the pre-mapped landslides (yellow) and a red point in correspondence to the center of the patches predicted as *Landslide*. The step of the window is 2 pixels. Patches are extracted with 25 x 25 pixels resolution and then resampled to match the input size of the network ($n \times 32 \times 32 \times 3$).

All experiments were executed on a mac-OS operating system computer with a 2.2 GHz Intel Core i7 with 6 cores, a 256 GB SSD for quick access to applications and datasets, and RAM 16 Gb.

4 Results

4.1 Landslide Classification

Table 3: Accuracy, precision and recall of the CNN tested on eight different test datasets explained in Table 2. The best results achieved with SAR data are pointed out.

Dataset Name	Accuracy(%)	Precision(%)	Recall(%)
RGB	99.20	99.60	98.81
SSD	86.63	92.24	80.16
SSS	80.84	82.77	78.17
BAD	89.96	95.83	83.47
BAS	88.55	96.58	79.84
HHH	81.87	93.22	68.75
BAA	94.17	97.32	90.83
BAC	90.83	93.36	87.92
BAH	93.33	95.22	91.25

We trained each model for the optimal number of epochs and using the best learning rate that fitted each specific problem. Table 4.1 shows the results for different datasets. As expected, the model trained and tested on RGB optical images performs well, achieving the best results. Focusing on SAR datasets, the BAH and BAA achieved the highest overall accuracies, with 93.33% and 94.17%, respectively. Besides, the BAH, achieved also the highest recall, with a value of 91.25%. The two datasets enclosing the slope as a third band, SSS and BAS, generally achieved the lowest accuracies, with 80.84% and 88.55%, respectively. Lastly, considering the HHH and the BAA, which are composed of the same combination of bands but different polarization, results show that the VV polarization is more discriminating to detect landslides than the VH.

To accomplish a visual evaluation of the predictions of the best models trained in this study, we analyzed the entire study area through the process explained in Section 3.3. Figure 2 shows the resulting mapping obtained with the models trained on the BAA and BAH datasets.

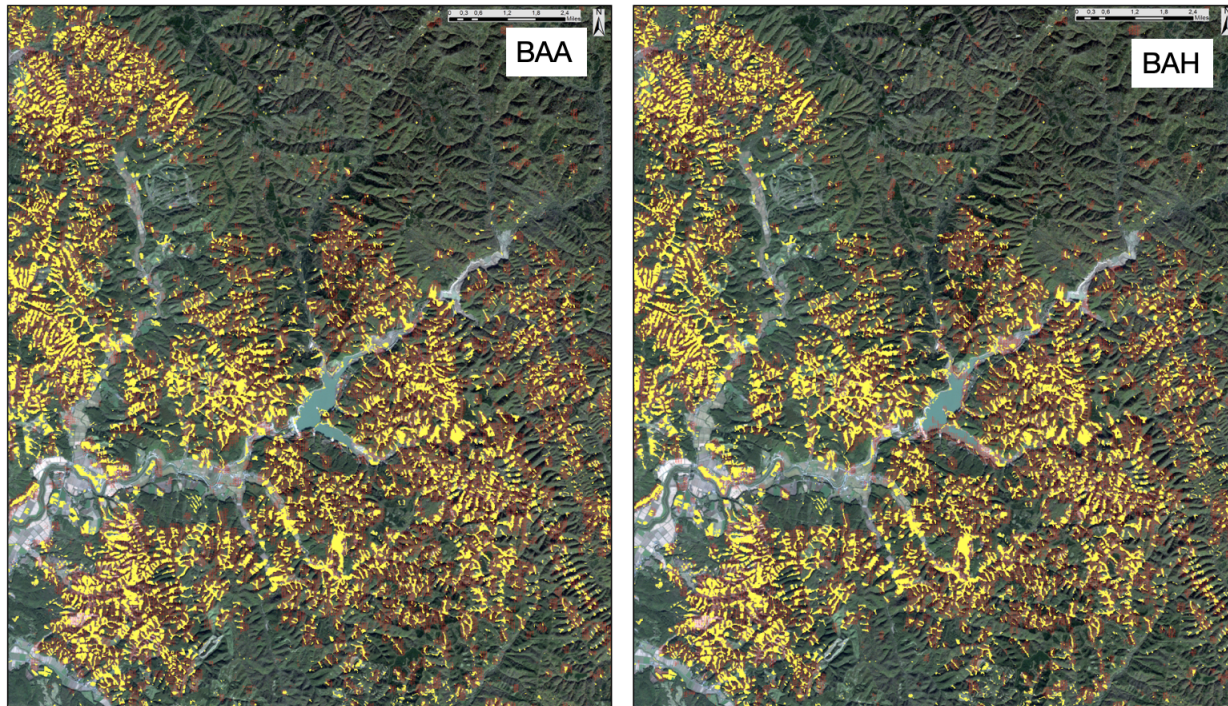


Figure 2: Predictions of the entire study area by the models trained on the BAA and BAH datasets. (BAA: Accuracy = 94.17%; Precision = 97.32%; Recall = 90.83%. BAH: Accuracy = 93.33%; Precision = 95.22%; Recall = 91.25%.)

5 Conclusion

In this letter, we analyzed and discussed various combinations of SAR imagery and topographic factors and we proposed a DL-based method for landslide detection to locate landslides in a short time, also during the night and in presence of cloud cover. The best overall accuracy was accomplished by the BAA and BAH datasets, composed just by three SAR bands. The accuracy of the latter was 94.17% and 93.33%, respectively, 5.03% and 5.87% less than with the RGB dataset, but with the advantage of being applicable also during storms or night. Therefore, it is possible to make a landslide detection without VHR optical images with similar accuracy values, using the combination of SAR data of the BAA or the BAH datasets. Moreover, VV and VH amplitude imagery from Sentinel-1 is an open-source product available in almost all parts of the globe. The results achieved so far in this letter are promising and suggest that SAR Sentinel-1 images and deep learning models are a trustworthy combination for locating rapid landslides. SAR images permit us to obtain information regarding landslides also during a rain event or during the night when optical imagery, instead, is unusable or not available because of the presence of cloud cover. Therefore, the method could involve also various benefits in terms of emergency management civil protection operations, such as significantly decreasing the time of the emergency response in various emergency scenarios by increasing the quality of hazard mapping and risk assessments.

References

- [1] Serey, A., Piñero-Feliciangeli, L., Sepúlveda, S.A. et al. "Landslides induced by the 2010 Chile megathrust earthquake: a comprehensive inventory and correlations with geological and seismic factors." *Landslides* vol. 16, pp. 1153–1165, 2019.
- [2] Song, K., Wang, F., Dai, Z. et al. "Geological characteristics of landslides triggered by the 2016 Kumamoto earthquake in Mt. Aso volcano." *Japan. Bull Eng Geol Environ* vol. 78, pp. 167–176, 2019.
- [3] Chunga, K., Livio, F.A., Martillo, C., Lara-Saavedra, H., Ferrario, M.F., Zevallos, I., Michetti, A.M. "Landslides Triggered by the 2016 Mw 7.8 Pedernales, Ecuador Earthquake: Correlations with ESI-07 Intensity, Lithology, Slope and PGA-h." *Geosciences*, vol. 9, pp. 371, 2019.
- [4] Wang, F., Fan, X., Yunus, A.P. et al. "Coseismic landslides triggered by the 2018 Hokkaido, Japan (Mw 6.6), earthquake: spatial distribution, controlling factors, and possible failure mechanism." *Landslides* vol. 16, pp. 1551–1566, 2019.
- [5] Ferrario, M.F. "Landslides triggered by multiple earthquakes: insights from the 2018 Lombok (Indonesia) events." *Nat Hazards* vol. 98, pp. 575–592, 2019.
- [6] H. Hong, W. Chen, C. Xu, A. M Youssef, B. Pradhan, D. Tien Bui. "Rainfall-induced landslide susceptibility assessment at the Chongren area (China) using frequency ratio, certainty factor, and index of entropy." *Geocarto Int.*, vol. 32, pp. 139-154, 2017.
- [7] F. Catani, D. Lagomarsino, S. Segoni, V. Tofani, "Landslide susceptibility estimation by random forests technique: sensitivity and scaling issues." *Nat. Hazards Earth Syst. Sci.*, vol. 13, 2815–2831, 2013.
- [8] B. Pradhan, "A comparative study on the predictive ability of the decision tree, support vector machine and neuro-fuzzy models in landslide susceptibility mapping using GIS." *Comput. Geosci.*, 51, 350–365, 2013.
- [9] L. Solway, "Socio-economic perspective of developing country megacities vulnerable to flood and landslide hazards." *Floods and Landslides: Integrated Risk Assessment*, Springer: Berlin, Heidelberg, pp. 245-260, 1999.
- [10] V. Svalova, "Landslide risk management for urbanized territories." *Risk Management Treatise for Engineering Practitioners*, Oduoza, C.F., Ed., IntechOpen: London, UK, pp. 1-19, 2018.
- [11] D. Myronidis, C. Papageorgiou, S. Theophanous, "Landslide susceptibility mapping based on landslide history and analytic hierarchy process (AHP)." *Natural Hazards*, vol. 81, pp. 245–263, 2016.
- [12] B. Feizizadeh, O. Ghorbanzadeh, "GIS-based interval pairwise comparison matrices as a novel approach for optimizing an analytical hierarchy process and multiple criteria weighting." *GI Forum*, vol. 1, pp. 27–35, 2017.
- [13] W. Chen, X. Xie, J. Wang, B. Pradhan, H. Hong, D. T. Bui, Z. Duan, J. Ma, "A comparative study of logistic model tree, random forest, and classification and regression tree models for spatial prediction of landslide susceptibility." *Catena*, vol. 151, pp. 147–160, 2017.
- [14] Y. Aimaiti, W. Liu, F. Yamazaki, Y. Maruyama, "Earthquake-induced landslide mapping for the 2018 Hokkaido Eastern Iwate Earthquake Using PALSAR-2 data." *Remote Sensing*, vol. 11, p. 2351, 2019.
- [15] Reichenbach, P., Rossi, M., Malamud, B. D., Mihir, M., and Guzzetti, F. "A review of statistically-based landslide susceptibility models." *Earth-Science Reviews*, vol. 180, pp. 60-91, 2018.
- [16] S. Voigt, T. Kemper, T. Riedlinger, R. Kiefl, K. Scholte, H. Mehl, "Satellite image analysis for disaster and crisis-management support." *IEEE Trans. Geosci. Remote Sens.*, vol. 45, pp. 1520–1528, May 2007.
- [17] M. Långkvist, A. Kiselev, M. Alirezaie, A. Loutfi, "Classification and segmentation of satellite orthoimagery using convolutional neural networks." *Remote Sens.*, vol. 8, p. 329, 2016.
- [18] M. Radovic, O. Adarkwa, Q. Wang, "Object recognition in aerial images using convolutional neural networks." *J. Imaging*, vol. 3, p. 21, 2017.
- [19] A. Ding, Q. Zhang, X. Zhou, B. Dai, "Automatic recognition of landslide based on CNN and texture change detection." *Proceedings of the Chinese Association of Automation (YAC)*, Youth Academic Annual Conference, Wuhan, China, 11–13 November 2016; IEEE: Wuhan, China, pp. 444–448, 2016.
- [20] O. Ghorbanzadeh, T. Blaschke, K. Gholamnia, S. R. Meena, D. Tiede, J. Aryal, "Evaluation of Different Machine Learning Methods and Deep-Learning Convolutional Neural Networks for Landslide Detection." *Remote Sens.*, vol. 11, p. 196, 2019.
- [21] F. Catani, "Landslide detection by deep learning of non-nadir and crowdsourced optical images." *Landslides*, vol. 18, pp. 1025-1044, 2020.

- [22] A. M. Wilson, W. Jetz, "Remotely Sensed High-Resolution Global Cloud Dynamics for Predicting Ecosystem and Biodiversity Distributions." *PLoS Biology*, vol. 14, p.e1002415, 2016.
- [23] J. G. Williams, N. J. Rosser, M. E. Kinsey, J. Benjamin, K. J. Oven, A. L. Densmore, D. G. Milledge, T. R. Robinson, C. A. Jordan, T. A. Dijkstra, "Satellite-based emergency mapping using optical imagery: Experience and reflections from the 2015 Nepal earthquakes." *Nat. Hazards Earth Syst. Sci.*, vol. 18, pp. 185–205, 2018.
- [24] A. C. Mondini, M. Santangelo, M. Rocchetti, E. Rossetto, A. Manconi, O. Monserrat, "Sentinel-1 SAR Amplitude Imagery for Rapid Landslide Detection." *Remote Sens.*, vol. 11, p. 760, 2019.
- [25] A. C. Mondini, F. Guzzetti, K. T. Chang, O. Monserrat, T. R. Martha, A. Manconi, "Landslide failures detection and mapping using Synthetic Aperture Radar: Past, present and future." *Earth-Science Reviews*, p. 103574, 2021.
- [26] K. Matsuno, M. Ishida, "Geological map of Hayakita in scale of 50,000." *Geological survey of Japan*, Tokyo, Japan, 1960.
- [27] N. Osanai, T. Yamada, S. Hayashi, S. Kastura, T. Furuichi, S. Yanai, Y. Murakami, T. Miyazaki, Y. Tanioka, S. Takiguchi, M. Miyazaki, "Characteristics of landslides caused by the 2018 Hokkaido Eastern Iburi Earthquake." *Landslides*, vol. 16, pp. 1517–1528, 2019.
- [28] "The 2018 Hokkaido eastern Iburi earthquake: fault model (preliminary)." Geospatial Information Authority of Japan, *GSI* 2018. [Online]. Available: <https://www.gsi.go.jp/cais/topic180912-index-e.html>
- [29] H. Yamagishi, F. Yamazaki, "Landslides by the 2018 Hokkaido Iburi-Tobu Earthquake on September 6." *Landslides*, vol. 15, pp. 2521–2524, 2018.
- [30] Sentinel-1, Sentinel Online, The European Space Agency. Available online: <https://sentinel.esa.int/web/sentinel/missions/sentinel-1/overview> (accessed on 16 February 2021).
- [31] Sentinel-2, Sentinel Online, The European Space Agency. [Online]. Available: <https://sentinel.esa.int/web/sentinel/missions/sentinel-2>
- [32] ESA. Copernicus Open Access Hub. [Online]. Available: <https://scihub.copernicus.eu/dhus/#/home>
- [33] Level-1 GRD Products, The European Space Agency. [Online]. Available: <https://sentinel.esa.int/web/sentinel/technical-guides/sentinel-1-sar/products-algorithms/level-1-algorithms/ground-range-detected>
- [34] J. A. Coe, J. W. Godt, R. L. Baum, R. C. Bucknam, J. A. Michael, "Landslide susceptibility from topography in Guatemala." *Landslides: Evaluation and Stabilization*, vol. 1, pp. 69–78, 2004.
- [35] USGS. Earth Explorer. [Online]. Available: <https://earthexplorer.usgs.gov/>
- [36] A. Krizhevsky, I. Sutskever, G.E. Hinton, "Imagenet classification with deep convolutional neural networks." *Advances in Neural Information Processing Systems*, vol. 25, pp.1097–1105, 2012.
- [37] H. C. Shin, H. R. Roth, M. Gao, L. Lu, Z. Xu, I. Nogues, J. Yao, D. Mollura, R. M. Summers, "Deep convolutional neural networks for computer-aided detection: CNN architectures, dataset characteristics and transfer learning." *IEEE Trans. Med. Imaging*, vol. 35, pp. 1285–1298, February 2016.
- [38] P. Marcelino, "Transfer learning from pre-trained models." *Towards Data Science*, October 2018.
- [39] D. Strigl, K. Kofler, S. Podlipnig, "Performance and scalability of GPU-based convolutional neural networks." *2010 18th Euromicro International Conference on Parallel, Distributed and Network-Based Processing. IEEE*, pp. 317–324, 17 February 2010.
- [40] Image Classification, Tensorflow Core Tutorial, Tensorflow. [Online]. Available: <https://www.tensorflow.org/tutorials/images/classification>
- [41] D. P. Kingma and J. Ba. "Adam: A method for stochastic optimization." Unpublished paper, 2014. [Online]. Available: <https://arxiv.org/abs/1412.6980>
- [42] Sparse Categorical Crossentropy, Tensorflow Core v2.4.1, Tensorflow. [Online]. Available: https://www.tensorflow.org/api_docs/python/tf/keras/losses/SparseCategoricalCrossentropy
- [43] M. Abadi et al. "TensorFlow: Large-scale machine learning on heterogeneous distributed systems." Unpublished paper, 2016. [Online]. Available: <https://arxiv.org/abs/1603.04467>.
- [44] C. H. Lee, C. R. Lin, M. S. Chen, "Sliding-Window Filtering: An Efficient Algorithm for Incremental Mining". *Proceedings of the tenth international conference on Information and knowledge management*, pp. 263–270, October 2001.